Composites: Part B 67 (2014) 381–390

Contents lists available at ScienceDirect

Composites: Part B

journal homepage: www.elsevier.com/locate/compositesb

Numerical optimization of strengthening disturbed regions of dapped-end beams using NSM and EBR CFRP

Gabriel Sas [a], Cosmin Dăescu [b,*], Cosmin Popescu [c], Támas Nagy-György [b]

[a] NORUT, Rombaksveien E-6 47, N-8517 Narvik, Norway
[b] Politehnica University of Timisoara, 2nd T. Lalescu, 300223 Timisoara, Romania
[c] Luleå University of Technology, SE-97187 Luleå, Sweden

ARTICLE INFO

Article history:
Received 17 April 2014
Received in revised form 21 June 2014
Accepted 8 July 2014
Available online 5 August 2014

Keywords:
A. Carbon fibre
B. Stress concentrations
C. Finite element analysis (FEA)
Retrofit

ABSTRACT

This paper presents a parametric investigation, based on non-linear finite element modeling, to identify the most effective configuration of carbon fiber-reinforced polymers (CFRP) for strengthening reinforced concrete (RC) dapped-end beams. Following a field application and laboratory tests, it focuses on effects of 24 externally bonded (EBR) and near surface mounted reinforcement (NSMR) configurations on yield strain in steel and the capacity and failure mode of dapped-end beams. The investigated parameters were the mechanical properties of the CFRP, the strengthening procedure and the inclination of the fibers with respect to the longitudinal axis. Two failure scenarios were considered: rupture and debonding of the FRP. The results indicate that high-strength NSM FRPs can considerably increase the capacity of dapped-end beams and the yielding strains in reinforcement can be substantially reduced by using high modulus fibers.

1. Introduction

1.1. Literature review

Effective construction using precast components is reliant on their standardization and design practicality. These elements may be linear (beams, columns), planar (walls, floors) or spatial sub-assemblages (beam-column nodes, pad foundations). In order to reduce the floor height and to facilitate the connection between beams and columns, dapped-end beams are generally used in precast concrete industry. As beams are generally placed on corbels or directly on columns severe reduction of the cross-section at their ends (dapped-ends) may be required, resulting in a complex flow of internal stresses, typically highly concentrated at the re-entrant corners. Such regions in an element are called disturbed regions (D-regions) [1,2]. Currently empirical methods are applied for designing D-regions, the standard used in design guidelines being the strut-and-tie model [2–4]. Using this approach, various authors Reynolds [5], Mattock [6], Mattock and Theryo [7], Hwang and Lee [8], Chen et al. [9], Lu et al. [10] Yang et al. [11] have proposed design models for dapped-end beams, all of which have yielded less conservative results than provisions in codes [3] or design guidelines [2].

The load carrying capacity (hereafter capacity) of dapped-ended beams may be affected by: design errors, code changes and structural damage. One method that can be used to increase their capacity is to apply externally bonded (EBR) or near surface mounted (NSM) fiber-reinforced polymers (FRP). Several guidelines for designing and applying FRPs as strengthening systems for RC structures have been published recently [12–14]. However, strengthening of D-regions with FRPs is marginally addressed in these guidelines due to lack of experimental and theoretical investigations on the variations in geometry, materials and loading conditions. Only few investigations of the FRPs effects on disturbed regions are reported in literature [15–18]. Gold et al. [15] tested several FRP-strengthened dapped-end beams used in a three-story parking garage, and found they had double the capacity of reference specimens. Tan [16] investigated effects of various types of FRPs on the capacity of dapped-end beams with deficient shear resistance and showed that tested mechanical anchorage devices improved the FRP systems' strengthening by preventing debonding. He also derived an empirically based strut-and-tie model that proved to be sufficiently accurate for predicting the shear capacity of the tested beams. Taher [17] tested 50 small-scale dapped-ends strengthened with various techniques and found that FRPs were the most viable solution for strengthening/retrofitting

* Corresponding author. Tel.: +40 256403935.
E-mail addresses: gabriel.sas@norut.no (G. Sas), cosmin.daescu@upt.ro (C. Dăescu), cosmin.popescu@ltu.se (C. Popescu), tamas.nagy-gyorgy@upt.ro (T. Nagy-György).

http://dx.doi.org/10.1016/j.compositesb.2014.07.013
1359-8368/

applications. He also derived a regression model for estimating the capacity of the FRP-strengthened dapped-end beams, which reportedly provided "reasonable predictions", but did not consider any possible scaling effects on the tested beams. In a series of tests Huang and Nanni [18] determined whether FRPs can increase the capacity of dapped-end beams with "mild steel and no mild reinforcement", and proposed a method for strengthening dapped-end beams with FRPs which was found to be "satisfactory and conservative". However, more knowledge of the effects of variations in geometry, materials and loading conditions on the strengthening of D-regions with FRPs is clearly required to identify optimal solutions.

1.2. The case study

Field work was conducted, in 2003, in an industrial hall being built using 20 m span precast prestressed RC beams with dapped-ends, each designed to resist a reaction force of 800 kN positioned 400 mm from the re-entrant corner. Diagonal cracks appeared in eight beams, starting from the re-entrant corner. Errors in assembly required a 275 mm shift in the position of the support. The new lever arm that resulted (675 mm) produced a capacity deficit of ca. 200 kN. To prevent further cracking and realise the desired capacity, a strengthening solution designed using linear (FEM) and strut-and-tie models. This consisted of externally bonding CFRP plates at 0° and 90° to the longitudinal axis of the beam (except for one beam, where purlins obstructed the 0°/90° arrangement, necessitating the use of a 45°/90° geometry). This layout provided the longest possible anchorage length and avoided debonding. The mechanical properties of the CFRP plates, denoted PS, are presented in Table 1. In designing the strengthening the strains in CFRP were limited to 4‰, according to the prescriptions given in fib Bulletin 14 [14].

1.3. Experimental program and initial FEM results

Two full scale beams were built, each with two dapped-ends, and tested in laboratory environment [19]. The arrangement, spacing, diameter and strength class of the reinforcements were identical to those of the original beams (see Fig. 1 and Table 2). The loads were applied incrementally, in 50 kN steps, in a force-control regime. The test setup is schematically presented in Fig. 2.

Firstly, a reference specimen was tested up to failure (C1). The remaining three dapped-ends (denoted C2, C3 and C4) were tested up to 800 kN, corresponding to the design load of the original dapped-ends. The pre-cracked elements were strengthened using three solutions (see Fig. 3). Two consisted of CFRP plates, applied in 45°/90° (RC2) and 0°/90° (RC4) orientations, as used in the field application (denoted "...- LAB" in Fig. 4). The overall behavior of the elements retrofitted with these two systems was found to be similar. The third system used consisted of CFRP fabrics aligned at 0°/45°/90° (RC3). The retrofitted systems were found to provide higher capacity and stiffness than C1, and delayed the onset of crack formation. At an applied load of 800 kN the strain was reduced in the steel reinforcements, relative to the reference specimen, by 31% for RC2 and 15% for both RC4 and RC3. Elements RC2 and RC4 failed due to debonding of the FRP, while element RC3 failed through rupturing of the CFRP fabrics. All three systems were also analyzed using numerical modeling (denoted "...- FEM" in Fig. 4). Very good agreement was found between numerical

Table 1
Mechanical properties and quantities of CFRPs used in modeling.

Material	PS	FM[a]	FS	PM	N1S	N1M	N2S	N2M
Width b (mm)	100	340	340	100	10	10	2.5	2.5
Thickness t[b] (mm)	1.2	0.19	0.17	1.4	10	10	20	20
Total no. of FRPs n (–)	4	8	6	6	6	6	10	10
FRP area/system (mm^2) [$n{\cdot}b{\cdot}t$]	480.0	516.8	346.8	840.0	600.0	600.0	500.0	500.0
Young modulus E (N/mm^2)	165,000	640,000	231,000	350,000	165,000	265,000	165,000	210,000
Ultimate strain ε_u (‰)	17	4	17	4.5	13.5	8.5	16.5	13
Strain at failure ε_{fail} (‰)	18	5	18	5.5	14.5	9.5	17.5	14
Variation vs PS (%) [$E{\cdot}\varepsilon_u{\cdot}n{\cdot}b{\cdot}t$]	0.00	−1.7	+1.2	−1.7	−0.7	+0.4	+1.1	+1.4
Strain at debonding ε_d (–)	0.0037	0.0023	0.0048	0.0023	0.0075	0.0059	0.0116	0.0103
Anchorage length l_a (mm)	238	373	183	374	173	220	130	146

[a] Strengthening system tested in the laboratory.
[b] Depth embedded into the concrete cover, see Fig. 5.

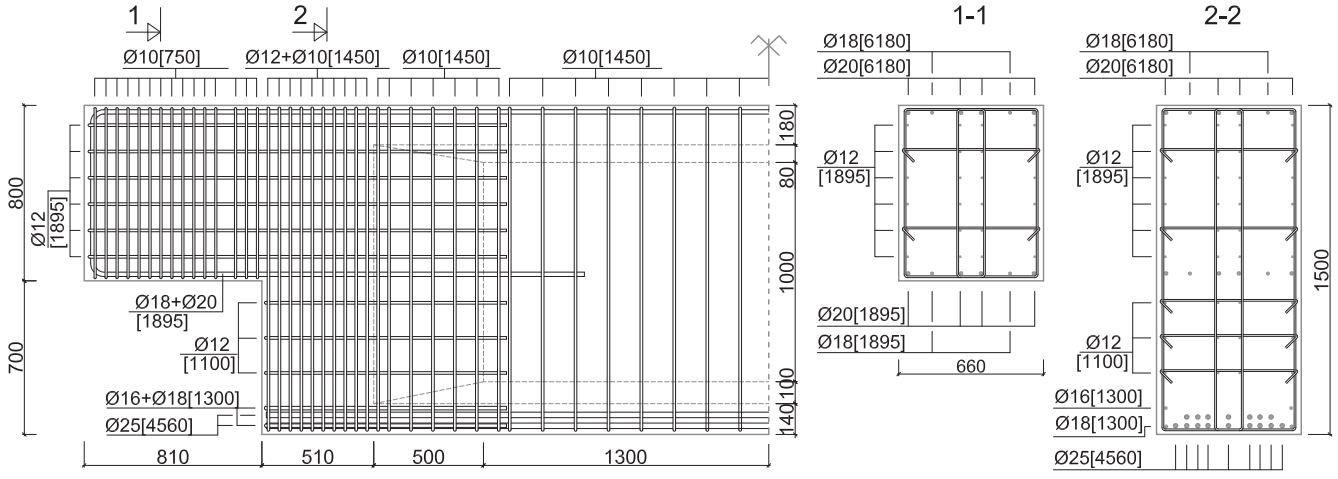

Fig. 1. Dimensions and layout of the steel reinforcement. Length of bars is given in brackets. All dimensions are in (mm).

Table 2
Properties of the steel material.

Diameter ϕ (mm)	Yield strength f_y (N/mm^2)	Tensile strength f_u (N/mm^2)	Yield strain ε_y (‰)	Ultimate strain ε_u (‰)	Strain at failure ε_{fail} (‰)
10	780	922	3.6	14.9	16.5
12	522	600	2.5	23.1	24.5
16/18/20	460	600	2.5	19.9	22.5
25	440	625	2.2	18.9	21.0

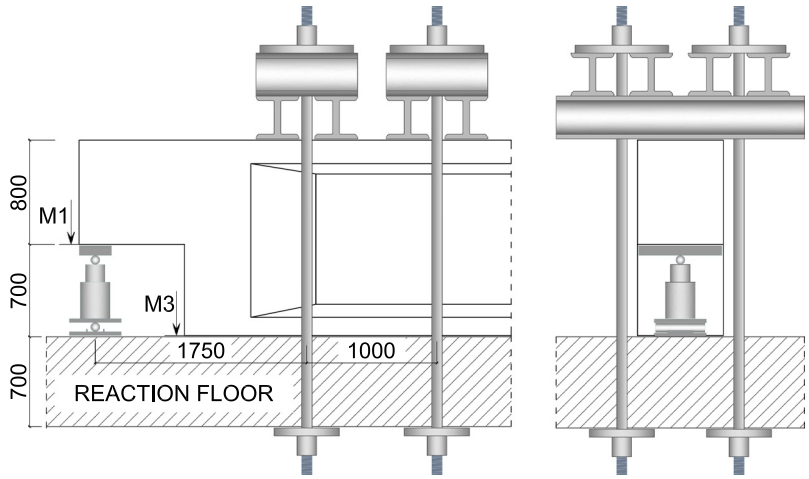

Fig. 2. Schematic illustration of the test set-up (units in mm).

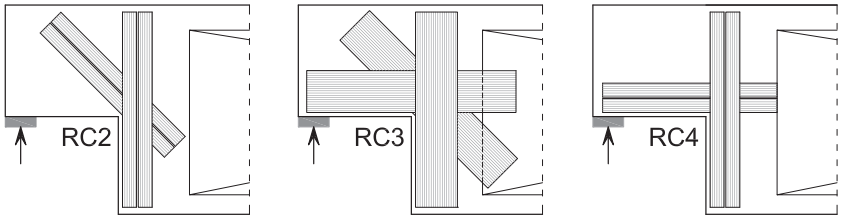

Fig. 3. Schematic illustration of the tested strengthening systems.

simulations and experimental results, as shown in Fig. 4. The debonding process and failure loads corresponding to FRP rupture were not modeled. Detailed descriptions of the experimental results are presented in Nagy-Gyorgy et al. [19] and Dăescu et al. [20]. The debonding was disregarded in the later study. In the present work, an indirect approach was used to evaluate the ultimate debonding load. Additionally, the parametric study includes high modulus (HM) FRPs. It was concluded also that the vertically applied CFRP components (90°) do not contribute to the capacity of the studied dapped-end beams. Thus they were omitted from further analysis.

The results confirmed the success of the FRP strengthening approach, as the strains at service limit states were effectively reduced. However, they also highlighted a need to elucidate the optimum system for strengthening such elements.

1.4. Scientific relevance

The work presented in this paper was motivated by the current dearth of experimental investigations into strengthening dapped-end beams using FRPs. To the authors' knowledge only four such investigations have been reported [15–18]. The reported FEM improves understanding of how EBR CFRPs contribute to the capacity of dapped-ends, and highlights critical FRP design aspects such as the choice of FRP material and orientation of the fibers. The numerical modeling approach presented in this paper identifies the most effective CFRP-based strengthening system and layout for the above field application. Effectiveness is discussed in terms of the ultimate capacity of the dapped-end beam and the strain reduction in the steel reinforcement.

2. Parameters investigated and design of the FRPs

The design variables that were investigated in this paper using FEM were chosen based on observations during the experimental work and preliminary numerical computations.

These variables are:

(a) The inclinations of the CFRP with respect to the longitudinal axis of the beam. Alignments of 0° and 45° were selected, in accordance with both the field application and experimental program.
(b) The mechanical properties of the CFRP materials. The experimentally tested beams were strengthened with high modulus (HM) and high strength (HS) FRPs. However, CFRP behavior with HS fabrics and HM plates was also included in the FEM study to obtain a more complete description of potential FRP strengthening.

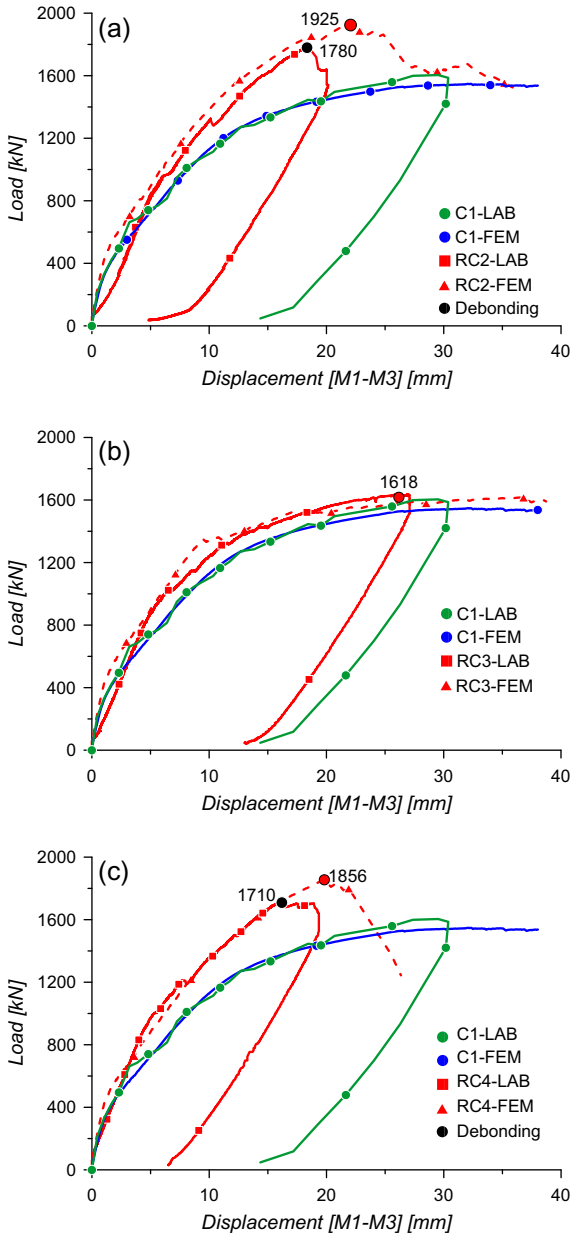

Fig. 4. Load deflection responses of the experimental and numerical systems tested. (a) C1 and RC2; (b) C1 and RC3; (c) C1 and RC4.

(c) CFRP layout application. Owing to the considerable increase in the use of NSMR strengthening over the past decade [21–23] the FEM investigation was extended to test the use of NSMR strengthening with both HS and HM fibers. Two types of NSMR cross-sections were selected, one rectangular and the other square, see Fig. 5, based on the prescriptions given in ACI 440.2R-08 [12] guidelines.

The fabrics, plates and NSM strengthening components are designated F, P and N, respectively. The mechanical properties of these components are named S for high strength and M for high modulus. The orientation of the applied CFRPs is denoted 00 for longitudinal and 45 for strengthening applied at 45° to the longitudinal direction. For example, FM45-N1M00 refers to a strengthening system composed of high modulus CFRP fabrics and type 1 high modulus NSMR bars applied at 45° and horizontally, respectively (see Table 1).

The CFRP fabrics and NSMR components used in the modeling were designed to have equivalent nominal strength along each direction to the CFRP strengthening systems used in the field application and laboratory tests. The number of CFRP layers (for fabrics), or elements (for plates and NSM), applied symmetrically to both faces of the element, designated n, and the required cross-section areas were obtained using Eq. (1). The Young-modulus (E) and the ultimate strain (ε_u) correspond to the mechanical properties of the CFRPs reported by their manufacturers. E_{PS}, A_{PS} and ε_{PS} are, respectively, the Young-modulus, cross-section area and ultimate strain of the CFRP strengthening system used in the field application and laboratory tests (PS in Table 1). Due to geometric limitations of the strengthened elements, the nominal strengths of CFRP sheets and NSM components are not identical to those of the CFRP plates, but the differences are minor (see Table 1).

$$n \cdot b \cdot t = \frac{A_{PS} \cdot E_{PS} \cdot \varepsilon_{PS}}{E \cdot \varepsilon_u} \quad (1)$$

3. FEM stages

This section presents the adopted investigation strategy for different strengthening solutions.

A two-stage strategy was applied to identify the optimum strengthening configuration. In the first stage, models for specific components of the strengthening systems were constructed and combined in all permutations. The results obtained for these simple cases allowed the construction of models covering the full range of feasible strengthening configurations. In the second stage, the individual CFRP components, applied at 0° and 45°, were combined (see Fig. 6). Owing to technological limitations imposed by the thinness of the concrete cover, the NSM bars can only be used in combination with either plates or fabrics. Thus, some solutions comprise a mix of EBR and NSM components, but are identified with N1 or N2 to facilitate distinction from the EBR systems.

3.1. Material characteristics

3.1.1. Concrete

The model of concrete behavior used in this analysis is based on a formulation by Cervenka and Papanikolaou [24,25] that combines constitutive models for tensile (fracturing) and compressive (plastic) behavior, (Fig. 7(a) and (b), respectively). In Fig. 7(b), f_{ct} is the tensile strength of concrete, G_f is the mode I fracture energy of concrete and w_c is the crack opening at the complete release of stress [25]. The fracture model is based on the classical orthotropic smeared crack formulation and crack band model. The latter assumes that crack spacing is larger than a finite element size. Using the program ATENA we set this parameter at 50 mm, based upon laboratory observations [19]. User-defined spacing is applied when it is smaller than an implicit crack band size derived by the software by projecting the size of the element in the crack direction, taking into consideration the angle between the direction of the normal to the failure plane and element side. According to Cervenka et al. [25] "the purpose of the failure band is to eliminate two deficiencies, which occur in connection with the application of the finite element model: element size effect and element orientation effect".

The fracture model employs the Rankine failure criterion using exponential softening, and it can be used for rotated or fixed crack models. The hardening/softening plasticity model is based on the Menétrey-Willam failure surface, using a return-mapping algorithm for the integration of constitutive equations. The plasticity model is combined with the fracture model through the use of an algorithm based on recursive substitution. This approach allows the two models to be formulated and developed separately. The

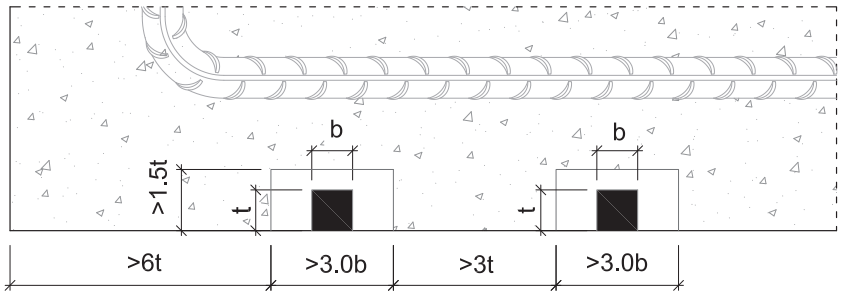

Fig. 5. Minimum geometrical requirements for NSMR application.

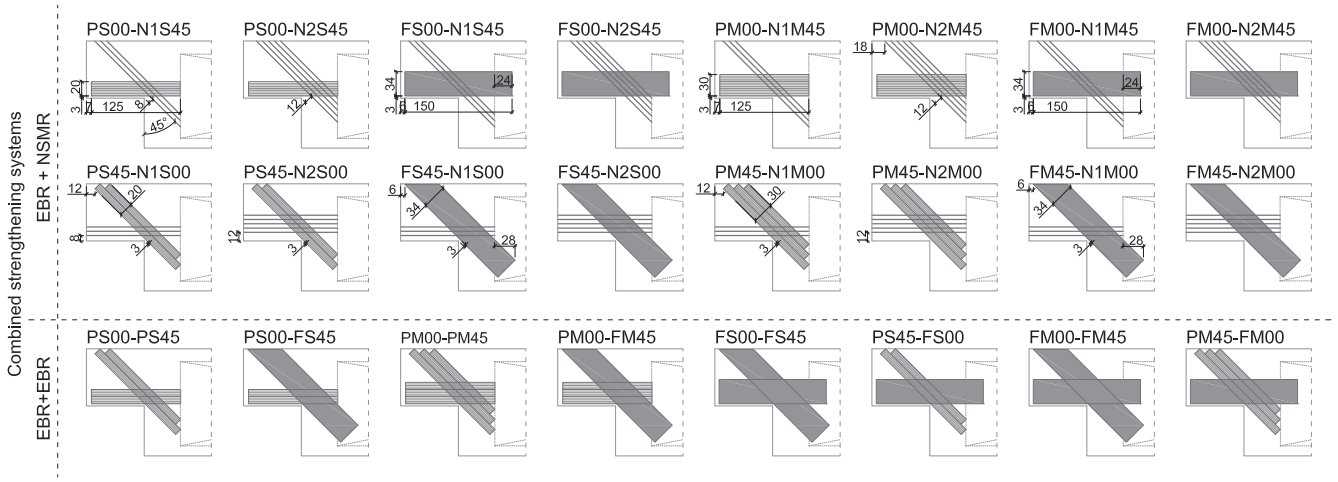

Fig. 6. Schematic illustration of the combined strengthening solutions.

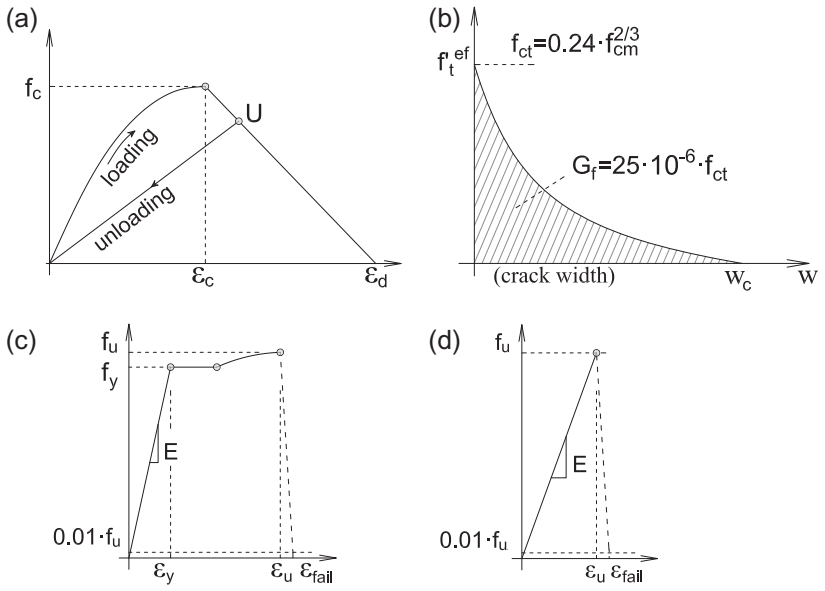

Fig. 7. Constitutive material models used in the numerical analysis. (a) Concrete compressive hardening/softening; (b) exponential crack opening law; (c) steel material model; (d) CFRP material model.

algorithm can describe cases in which failure surfaces are active for both models, and also when physical changes such as crack closure occur. The model can be used to simulate concrete cracking, crushing under high confinement, and crack closure due to crushing in other material directions.

The mechanical properties of the concrete were determined using standardized concrete cube tests. The mean compressive (f_{cm}) cube strength was found to be 56 MPa. Based on this value a compressive cylinder strength (f_c) of 47.6 MPa, a tensile strength (f_{ct}) of 3.51 MPa, an elastic modulus (E_c) of 38400 MPa, a fracture

energy (G_f) 87.8 N/m and a crack spacing (c_s) of 50 mm were all derived and used for FEM analysis.

3.1.2. CFRP and steel bars

Discrete bars were used to model the steel reinforcement and the NSM CFRP strengthening. Their characteristic behavioral curves are presented in Fig. 7(c and d). After the peak strength (f_u), the stress was reduced to 1% of f_u so that internal stress redistribution could be assured in the numerical computations. The values used for defining the stress–strain relationships are given in Tables 1 and 2. The cross-sectional area of one NSMR bar was defined as a discrete bar in the FEM calculations. The behavior of the CFRP fabrics and plates was modeled using the smeared reinforcement method.

3.2. Boundary conditions

The load was applied as an incrementally imposed deformation at one point through a metal plate with linear elastic properties. Displacements were monitored using FEM at locations where the linear variable differential transformers were installed on the tested beams. During laboratory tests the beams separated from the strong floor due to elastic deformation of the restraining test setup. This separation was accounted for in FEM by using contact elements.

The elastic deformation of the test setup was calibrated using the experimental results, and then integrated in all numerical simulations. The concrete floor was modeled as a linear elastic material.

3.3. Discretization into finite elements

A previous parametric investigation of mesh size effects on the accuracy of the FEM calculations revealed that a mesh resolution between 25 and 50 mm in the most heavily loaded section of the structure is sufficient for convergence [19]. The geometry of the simulated elements is discontinuous and therefore the triangular elements fitted better to cover drastic shape changes. Also, in order to save computational time, triangular elements were used rather than quadrilateral elements. The accuracy of the proposed FEM model was good as can be seen from Fig. 4a–c. As the web area and unloaded dapped-end of the beams were not structurally damaged during the laboratory tests a coarser mesh was deemed sufficient for the modeling presented here. Thus, these areas were discretized with 100, 150 and 250 mm element size triangular mesh, in order to reduce the computational time. The mesh dimensions used in the calculations are represented in Fig. 8.

3.4. Numerical methods

A standard incremental and iterative Newton–Raphson method is used to compute the model stiffness in the FEM. The Newton–Raphson equilibrium iterations provide convergence at the end of each load increment within defined tolerance limits. Before each solution, the solver assesses the out-of-balance load vector, which is the difference between the restoring forces (the loads corresponding to the element stresses) and the applied loads. Subsequently, the program seeks a linear solution using the out-of-balance loads and checks for convergence. If convergence criteria are not satisfied, the out-of-balance load vector is reevaluated, the stiffness matrix is updated and a new solution attained. This iterative procedure continues until the problem converges. In this study, four convergence criteria were used simultaneously: the norm of deformation changes during the last iteration, the norm of out-of-balance forces, out-of-balance energy and out-of-balance forces in terms of maximum components (rather than Euclid norms). The values of the convergence limits were set to 0.01 – see Cervenka et al. [25] for further details.

A triangular isoparametric 3-node element with one integration point was used for the plane stress representation. A Gaussian integration scheme with 1 integration point was used for all the concrete elements. The FEM model was constructed using 2D plane stress elements for the concrete and perfectly bonded embedded 2-nodes truss elements for the steel and NSM bars. The FRP fabrics and plates were introduced as smeared reinforcement in a special 2D RC element. In cases with overlapping fabrics or plates, two layers of smeared reinforcement were defined inside the same 2D RC element, at their corresponding inclination angles [25].

3.5. Limitations for interpreting failure modes in the numerical modeling

The nature of the numerical analysis, constructed as a 2D plain stress problem, coupled with the smeared strategy approach used to model the CFRP sheets and plates, precluded description of CFRP debonding from the concrete surface. In Atena, the constitutive model for bond slip describes the shear stress along a discrete bar. In the tests presented previously [19], the debonding took form of concrete rip-off, where all the concrete cover has been separated from the surface of the stirrups. To the authors' best knowledge, there is only one model [26] that can capture such failure mode. However, that model is derived on empirical basis thus not applicable to this study. Moreover, this is a parametric study; therefore it's hard to predict what type of debonding would occur for different FRP systems. Alternatively, the debonding load was determined by monitoring the debonding strain in the CFRPs and the anchorage length. These two parameters were determined using the procedures presented in Sas et al. [27] for EBR, and

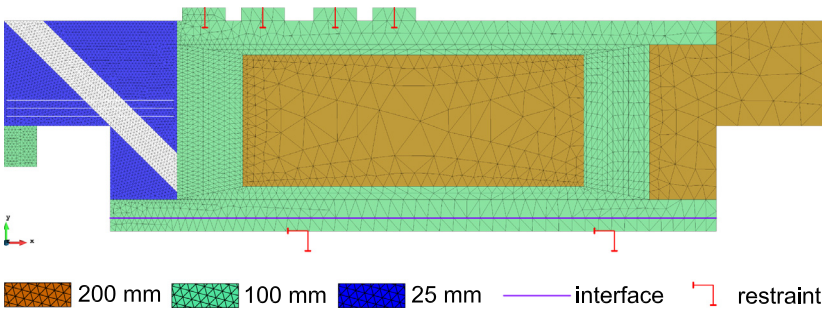

Fig. 8. Optimized mesh size obtained from the parametric study.

Mohamed Ali et al. [28] for NSM, respectively. These bond models are summarized in the following.

3.5.1. Bond model for NSM [28]

$$P_{deb} = \frac{\tau_f L_{per}}{\lambda} \tag{2}$$

$$\varepsilon_d = \frac{P_{deb}}{E_p b_p t_p} \tag{3}$$

and

$$\ell_{cr} = \frac{\pi}{2\lambda} \tag{4}$$

where,

$$\tau_f = 0.54\sqrt{f_c} b_p^{0.4} t_p^{0.3} \tag{5}$$

$$L_{per} \cong 2b_g + t_g \tag{6}$$

$$\lambda = \sqrt{\frac{\tau_f L_{per}}{\delta_f E_p t_p b_p}} \tag{7}$$

$$\delta_f = 0.78\left(\frac{f_c^{0.27}}{t_g^{0.3}}\right) \tag{8}$$

where P_{deb} – bond strength of the interface, ε_d – strain at debonding, ℓ_{cr} – critical bonding length, τ_f – peak shear stress at the interface, L_{per} – perimeter of the failure plane, λ – a constant, f_c – compressive strength of concrete, b_p, t_p – width and thickness of the NSM bar, b_g, t_g – depth and thickness of the groove, δ_f – the interface slip, E_p, Young's modulus of NSM bar,

3.5.2. Bond model for EBR plates and sheets [27]

$$\varepsilon_d = \sqrt{\frac{2G_f}{E_p t_p w}} \tag{9}$$

and

$$\ell_{cr} = \sqrt{\frac{E_p t_p}{2f_{ctm}}} \tag{10}$$

where

$$G_f = 0.644 f_c^{0.19} \tag{11}$$

where G_f – fracture energy defined by the stress–slip curve, f_{ctm} – mean tensile strength of concrete

For each type of CFRP the critical bonding length (ℓ_{cr}) and the debonding strain (ε_d) were determined, as shown in Fig. 9. The values estimated for these parameters are given in Table 1. These parameters were used to estimate the debonding load, which was considered to occur when the debonding strain, which developed over the entire width of the CFRP, was recorded at the location of the calculated anchorage length. Owing to the complex nature of the debonding process and its diverse manifestations (e.g. plate-end debonding, intermediate crack debonding, peeling-off and ripping-off), numerous models have been derived in attempts to describe it. There are considerable predictive discrepancies between these models, and it is possible that different models would yield different debonding loads for the cases considered here. However, the EBR and NSM models used for the results presented in this paper were selected because they are intuitive and provide conservative results.

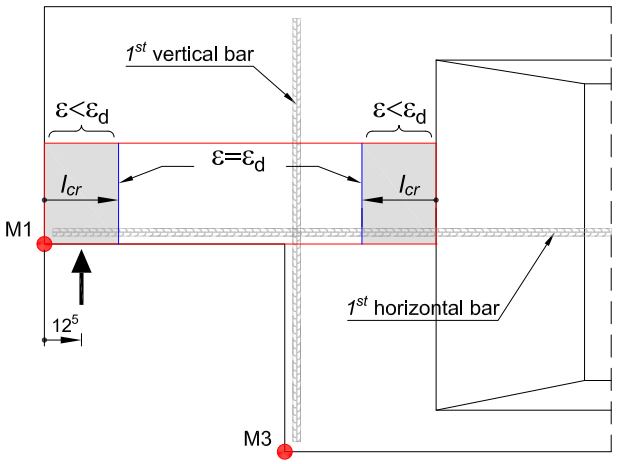

Fig. 9. Schematic representation of the monitored parameters from numerical analysis.

4. Assessment of the strengthening systems

The results of all analyzed models are presented in Table 3. Figs. 10–12 show load displacement diagrams generated from the numerical analysis. For clarity the general characteristics of these diagrams are described below. They are grouped according to the material properties of the FRP (HS vs HM) and type of CFRP strengthening technique used (EBR vs NSM). In order to facilitate comparisons of general strengthening behavior between groups, the envelope corresponding to the region between the maximum and minimum load curves has been highlighted. The point at which debonding is predicted to occur is indicated in each diagram. After this point the load increases to the maximum capacity of the CFRP strengthening system, and the corresponding part of the diagram simulates behavior in the region in which the CFRPs should be mechanically anchored. The debonding load represents the lowest bound capacity of the dapped-end beam, while the rupture load represents the highest bound capacity. When ultimate strain in the CFRP was reached, distributed over its entire width, the CFRP was considered to have failed by rupture. The results of the numerical analysis for each strengthening system are compared to the results obtained from the numerical analysis of the reference specimen (C1-FEM).

4.1. EBR: HM vs HS

The behavior of the EBR HM and HS systems is presented in Fig. 10(a) and (b). As expected and confirmed through laboratory tests on specimen RC3 (Fig. 4b), the HM fibers have limited capacity for deformation. Consequently, the elements strengthened using HM fiber systems, at ultimate strain, are able to provide modest gains in capacity compared to the reference specimen (C1-FEM, 1515 kN), about 13% in the best case scenario (specimen PM00-PM45; Table 3), and no increase in debonding load. Note, for specimens FM00-FM45 and PM00-FM45 the load at debonding is smaller than the ultimate capacity of the reference specimen. This inaccuracy is attributed to the conservative nature of the EBR model of Sas et al. [27].

The HS fiber systems were found to increase the capacity by up to 23%, with small variations in capacity, suggesting that the choice of fabrics and plates does not have a significant influence. However, there is a larger predicted variation in debonding load (14–28%; Table 3). For systems composed solely of HS fibers no debonding occurs. For the other three systems, containing plates, debonding always starts in the horizontal components, as they

Table 3
Results of the numerical simulations for strengthening systems.

Group type	Model	Load at failure of the FRP for… (kN)		Deb. load incr. (%)	Rupture load incr. (max load) (%)	Load at steel yielding (kN)		Increase in load at steel yielding (%)	
		Debonding	Rupture			1st vertical bar	1st horiz. bar	1st vertical bar	1st horiz. bar
(1)	(2)	(3)	(4)	(5)	(6)	(7)	(8)	(9)	(10)
Ref	C1-FEM	–	–	–	–	596	848	–	–
EBR-HS	FS00-FS45	–	1824[a,b]	–	20	807	1034	35	22
	PS00-FS45	1860[a]	1860[b]	23	23	704	949	18	12
	PS00-PS45	1725[a]	1858[b]	14	23	782	1010	31	19
	PS45-FS00	1785[a]	1846[b]	18	22	772	1191	30	40
EBR-HM	FM00-FM45	1496[b]	1682[a,b]	−3	11	751	1101	26	30
	PM00-FM45	1494[1]	1654[b]	−3	9	760	961	28	13
	PM00-PM45	–	1711[a]	–	13	796	1233	34	45
	PM45-FM00	1538[b]	1566[a]	2	3	788	914	32	8
N1-HS	FS00-N1S45	–	2031[b]	–	34	746	1124	25	33
	FS45-N1S00	1867[a]	1902[a]	23	26	757	1037	27	22
	PS00-N1S45	1829[a]	2011[b]	21	33	740	1057	7	25
	PS45-N1S00	1818[b]	1941[b]	24	28	791	1127	33	33
N1-HM	FM00-N1M45	1593[a]	1758[a]	5	16	859	1168	44	38
	FM45-N1M00	1643[b]	1799[a]	8	19	795	1095	33	29
	PM00-N1M45	1706[a]	1854[a]	13	22	703	1258	18	49
	PM45-N1M00	–	1730[b]	–	14	820	1109	38	31
N2-HS	FS00-N2S45	–	1980[b]	–	31	692	1066	16	26
	FS45-N2S00	1792[b]	1792[a]	18	18	757	1008	27	19
	PS00-N2S45	1929[a]	2053[b]	27	36	717	1019	20	20
	PS45-N2S00	1799[b]	1838[b]	16	21	784	1112	32	31
N2-HM	FM00-N2M45	1498[a]	1759[b]	−1	16	768	1062	29	25
	FM45-N2M00	1633[b]	1699[a]	8	12	784	1084	32	28
	PM00-N2M45	1542[a]	1862[b]	2	23	708	1260	19	49
	PM45-N2M00	–	1824[b]	–	20	807	1034	35	22

[a] Failure of the horizontal FRP component.
[b] Failure of the inclined FRP component. Column: (1) groups of FRP strengthening, (2) model denomination, (3) predicted load at debonding of the FRP component, (4) predicted load at rupture of the FRP component (also maximum capacity), (5) load capacity increase compared to reference specimen when debonding of FRP occurs, (6) load capacity increase compared to reference specimen when rupture occurs, (7 and 8) load at steel yielding in first vertical/horizontal bar from re-entrant corner, (9 and 10) increase in load at steel yielding in the first vertical/horizontal bar.

have shorter anchorage lengths than the 45° components. In terms of service limit both EBR HM and HS systems delay the yielding of the internal reinforcement (see columns 9 and 10 in Table 3), and can increase the yielding load by up to 45% compared to the reference specimen.

4.2. NSM: HM vs HS

The behavior of the N1 HM, N1 HS, N2 HM and N2 HS systems are presented in Figs. 11(a) and (b), 12(a) and (b), respectively. Generally, their behavior is similar to that of the EBR systems. In terms of ultimate failure load the HS NSM fibers outperform the HM fibers, for both types of cross-section investigated. Increases in debonding and rupture loads, relative to those of the reference specimen, of up to about 36% and 27% respectively, were recorded for element PS00-N2S45 (see Table 3), while the reinforcement yields at loads up to about 50% higher.

4.3. EBR vs NSM

The HM NSM systems (Figs. 11a and 12a), can provide higher increases in capacity than the HM EBR systems (Fig. 10a), but the HS EBR (Fig. 10b) systems provide the highest increases in ultimate capacity. The trend is similar for debonding loads. The loading of the first yielding in the reinforcement does not seem to be influenced by the type of strengthening system.

In terms of debonding loads, the HS EBR and HS NSM systems provide similar increases relative to the reference specimen (14–23% and 16–27%, respectively), while the HM EBR and HM NSM systems provide marginal increases (−3% to 2% and – to 13%, respectively). In terms of maximum force, the HS EBR and HS NSM systems provide significant increases (20–23% and 18–36%, respectively), the HM NSM systems provide a moderate increase (13–23%), and the HM EBR systems marginal increases (3–13%). In terms of delaying the first yield the increase was similar across the strengthening groups (except for PM45-FM00, PS00-N1S45 and PS00-N2S45), ranging from 12% to 45%. An early failure was recorded for the PM45-FM00 strengthening system (1711 kN), but the PS00-N1S45 and PS00-N2S45 systems provided the highest capacity gains (+33% and +36%, respectively) due to the yielding of the steel reinforcement (vertically aligned), which allowed advantageous stress redistribution.

4.4. N1. vs N2

The type of NSM cross-section used, see Table 1, governs the positioning of the CFRP with respect to the most heavily loaded section of the dapped-end and the number of bars used. The results show that differences in ultimate capacity loads between systems with the two types of cross-section are marginal. Element PS00-N2S45, with the rectangular cross-section N2S ($2.5 \times 20\ mm^2$), provided the largest gain (36%), while the best performing element with a square cross-section (N1S, $10 \times 10\ mm^2$) provided a 33% gain. Nevertheless, all of the HS NSM systems provide both greater capacity gains than the HM NSM counterparts (18–36% and 12–23%, respectively) and debonding load gains (16–27% and −1% to 13%, respectively). However, in terms of delaying the first yield, the HM NSM systems (except PM45-N1M00, as discussed above) can provide a more consistent increase than the HS NSM systems

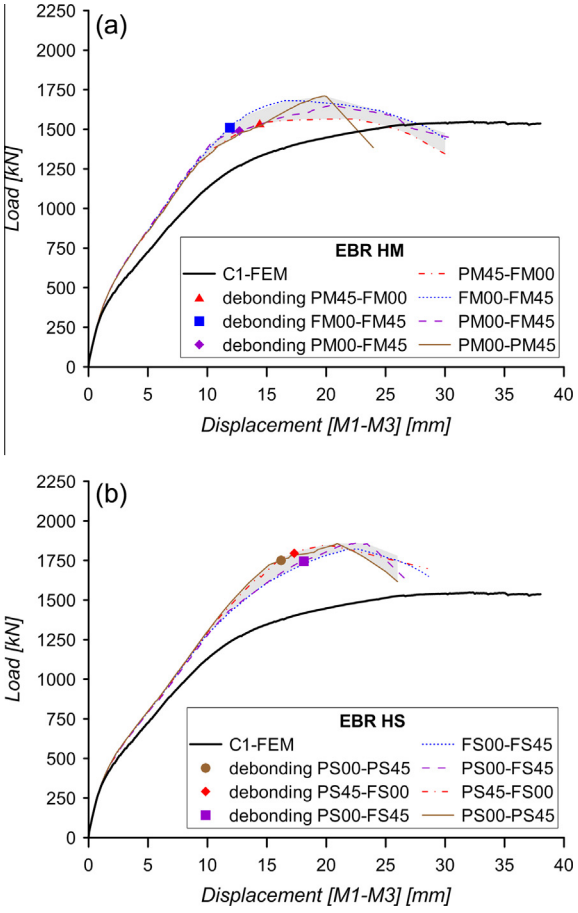

Fig. 10. Load displacement diagrams for the (a) EBR-HM group; (b) EBR-HS group.

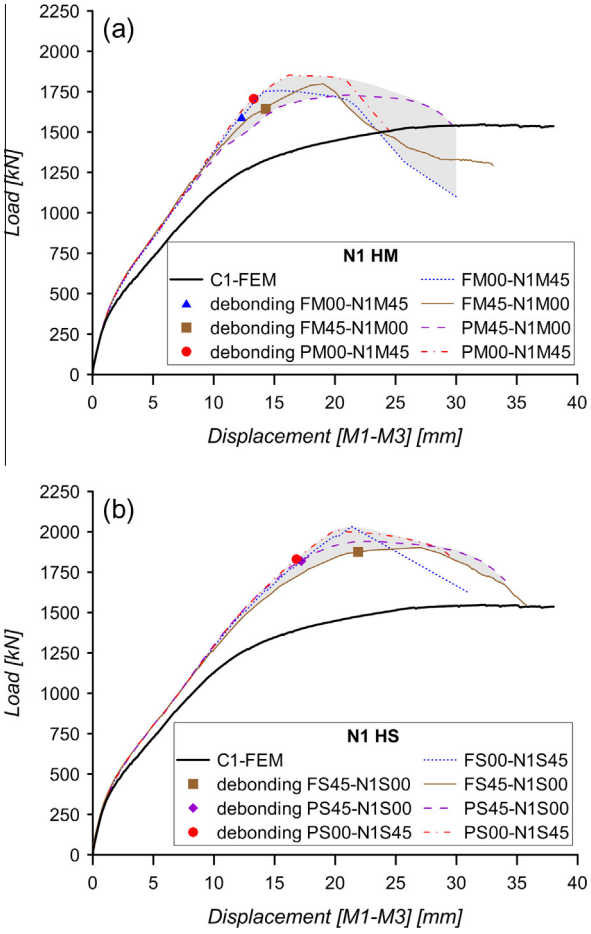

Fig. 11. Load displacement diagrams for the (a) N1-HM group; (b) N1-HS group.

(except PS00-N1S45 and PS00-N2S45, 19–49 and 16–33% gains, as also previously described).

5. Discussion and conclusions

The theoretical study presented in this paper was motivated by an experimental case project aimed at strengthening dapped-end beams. The choice of FRP materials available at that time (2003) provided two possible strengthening systems. To verify the efficiency of the applied systems, a series of tests and numerical simulations were carried out. Numerical modeling showed excellent agreement with the experimental test data.

As only two strengthening systems were experimentally tested in the field application an important question remained, namely whether an alternative arrangement could further improve the ultimate capacity of the beams. Thus, in the study presented here all strengthening configurations that could have been applied in practice were investigated in numerical simulations. The modeling approach was to combine CFRPs with different mechanical properties and shapes but similar alignments to tested specimens (0° and 45°). The results indicate that mechanically anchoring the CFRP (as in the PS00-N2S45 arrangement) could have increased the beams' capacity, relative to that of the reference specimen, by up to 36%. The PS00-N2S45 configuration outperforms the two systems used in the field application, RC2 and RC4, with increases in capacity of 20.7% and 16.1% respectively.

The debonding process was not modeled, because the modeling was carried out in 2D. In a 3D analysis debonding could be modeled, using a bond slip law or a cohesion–friction model. This was not done due to a lack of the empirical information required to calibrate the constitutive model. All the results presented above are based on perfect connections and anchorages between the strengthening systems and the concrete element. The occurrence of debonding was simulated by monitoring the strains and the characteristic bond length in the FRP. These parameters were evaluated using existing models available in the literature. Estimating the debonding process in such manner is model-dependent due to the details of the theoretical models used, not because of the numerical modeling. If debonding does occur the maximum load, relative to that of the reference specimen, could be increased by up to about 26% using the PS00-N2S45 system, which outperforms the strengthening configurations used in the case study. Element RC2 failed by debonding at 1760 kN, whereas the PS00-NS245 element could resist a load of about 1930 kN before debonding.

In some cases the debonding load was close to the rupture load of the FRP. This indicates that for these strengthening systems the anchorage length was nearly sufficient to avoid debonding.

One objective of the field work was to delay yielding initiation into the steel reinforcement. The numerical analysis has shown that this can been achieved to a certain degree with any of the strengthening configurations investigated. The force at which yielding first occurs can be increased by up to almost 50%, depending mainly on the type of fibers used and their position with respect to the reentrant corner. In this respect high modulus fibers are better than high strength fibers, because of their greater stiffness. In addition, the closer to the edge the FRP is applied the sooner it starts to be loaded.

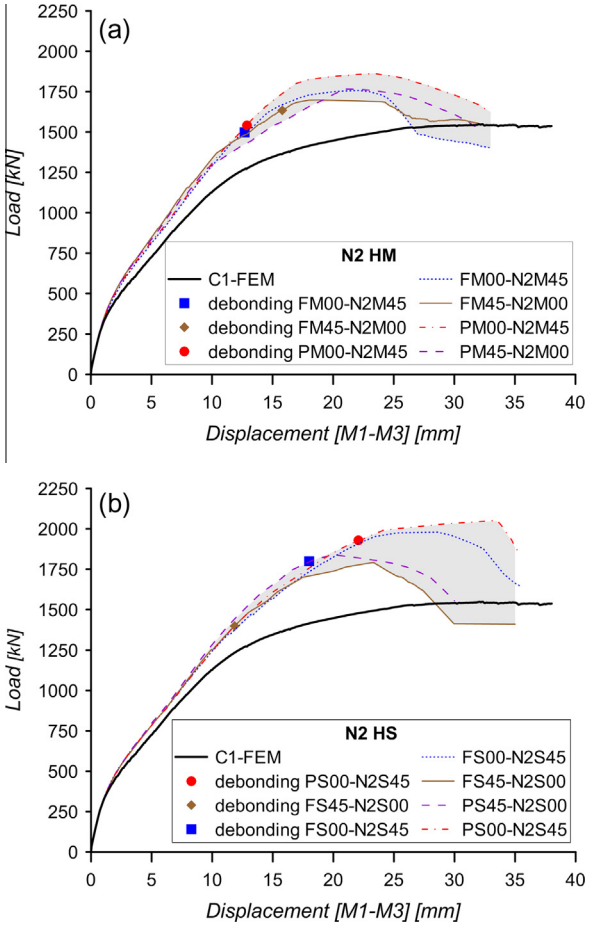

Fig. 12. Load displacement diagrams for the (a) N2-HM group; (b) N2-HS group.

The results presented here show that the applied strengthening systems, based on CFRP, are viable solutions for improving the capacity of dapped-end beams, especially when, as in the case of NSM, a large part of the strengthening system is applied as close to the beams' re-entrant corners as possible.

References

[1] ASCE-ACI Committee 445. Recent approaches to shear design of structural concrete. J Struct Eng-ASCE 1998; 124(12): 1375–417.
[2] PCI. PCI design handbook: precast and prestressed concrete. Illinois: Ed. (MNL 120-04); 2004.
[3] ACI Committee 318. Building code requirements for structural concrete (ACI 318-11) and commentary. Farmington Hills: American Concrete Institute; 2011.
[4] EN 1992-1-1. Eurocode 2: design of concrete structures – Part 1-1: General rules and rules for buildings. Brussels: COMITÉ EUROPÉEN DE NORMALISATION; 2004.
[5] Reynolds GC. The strength of half-joints in reinforced concrete beams. London: Cement and Concrete Association; 1969.
[6] Mattock AH. Design and behavior of dapped-end beams. J Prestr Concr I 1979;24(6):28–45.
[7] Mattock AH, Theryo TS. Strength of precast prestressed concrete members with dapped ends. J Prestr Concr I 1986:58–75.
[8] Hwang SJ, Lee HJ. Strength prediction for discontinuity regions by softened strut-and-tie model. J Struct Eng-ASCE 2002;128(12):1519–26.
[9] Chen BS, Hagenberger MJ, Breen JE. Evaluation of strut-and-tie modeling applied to dapped beam with opening. ACI Struct J 2002;99(4):445–50.
[10] Lu WY, Lin IJ, Hwang SJ, Lin YH. Shear strength of high-strength concrete dapped-end beams. J Chin Inst Eng 2003;26(5):671–80.
[11] Yang KH, Ashour AF, Lee JK. Shear strength of reinforced concrete dapped-end beams using mechanism analysis. Mag Concr Res 2011;63(2):81–97.
[12] ACI 440.2R-08. Guide for the design and construction of externally bonded FRP systems for strengthening concrete structures. Farmington Hills: American Concrete Institute; 2008.
[13] CNR DT200. Guide for the design and construction of externally bonded FRP systems for strengthening existing structures. Rome: Italian National Research Council; 2004.
[14] Fib Bulletin 14. Externally bonded FRP reinforcement for RC structures. Lausanne: International Federation for Structural Concrete; 2001.
[15] Gold WJ, Blaszak GJ, Mettemeyer M, Nanni A, Wuerthele MD. Strengthening dapped ends of precast double tees with externally bonded frp reinforcement. In: Elgaaly M, editor. ASCE Structures Congress. Philadelphia 2000. p. 9, CD version #40492-045-003.
[16] Tan KH. Shear strengthening of dapped beams using FRP systems. In: Burgoyne C, editor. FRPRCS-5. Cambridge: Thomas Telford Ltd; 2001. p. 249–58.
[17] Taher S. Strengthening of reentrant corner zone in recessed RC beams. In: El-Nahhas F, Dessouki A, Soliman E, Saad F, editors. Eleventh International Colloquium on Structural and Geotechnical Engineering. Cairo; 2005.
[18] Huang PC, Nanni A. Dapped-end strengthening of full-scale prestressed double tee beams with FRP Composites. Adv Struct Eng 2006;9(2):293–308.
[19] Nagy-Gyorgy T, Sas G, Daescu AC, Barros JAO, Stoian V. Experimental and numerical assessment of the effectiveness of FRP-based strengthening configurations for dapped-end RC beams. Eng Struct 2012;44:291–303.
[20] Dăescu AC, Nagy-György T, Sas BG, J.A.O. B, Popescu C. Assessment of the strengthening effectiveness of EBR and NSM techniques for beams' dapped-end by FEM analysis. In: Barros JS-C, J., editor. 11th International Symposium on Fiber Reinforced Polymers for Reinforced Concrete Structures (FRPRCS-11), Guimarães, Portugal: University of Minho; 2013. p. 1–9.
[21] Bianco V, Barros JAO, Monti G. Three dimensional mechanical model for simulating the NSM FRP strips shear strength contribution to RC beams: parametric studies. Eng Struct 2009;31(4):815–26.
[22] De Lorenzis L, Teng JG. Near-surface mounted FRP reinforcement: an emerging technique for strengthening structures. Composites Part B 2007;38(2):119–43.
[23] Rizzo A, De Lorenzis L. Behavior and capacity of RC beams strengthened in shear with NSM FRP reinforcement. Constr Build Mater 2009;23(4):1555–67.
[24] Cervenka J, Papanikolaou VK. Three dimensional combined fracture-plastic material model for concrete. Int J Plast 2008;24(12):2192–220.
[25] Cervenka V, Jendele L, Cervenka J. ATENA program documentation. Part 1: Theory. Cervenka Consulting Ltd; 2012.
[26] Aprile A, Feo L. Concrete cover rip-off of R/C beams strengthened with FRP composites. Composites Part B 2007;38(5–6):759–71.
[27] Sas G, Carolin A, Täljsten B. A model for predicting the shear bearing capacity of FRP-strengthened beams. Mech Compos Mater 2008;44(3):245–56.
[28] Mohamed Ali MS, Oehlers DJ, Griffith MC, Seracino R. Interfacial stress transfer of near surface-mounted FRP-to-concrete joints. Eng Struct 2008;30(7):1861–8.